Computers and Mathematics with Applications 130 (2023) 105–118

Contents lists available at ScienceDirect

Computers and Mathematics with Applications

journal homepage: www.elsevier.com/locate/camwa

An interpolation-free cell-centered discretization of the heterogeneous and anisotropic diffusion problems on polygonal meshes

Shuai Miao [a,b], Jiming Wu [b,*], Yanzhong Yao [b]

[a] Graduate School of China Academy of Engineering Physics, Beijing, 100088, PR China
[b] Institute of Applied Physics and Computational Mathematics, Beijing, 100088, PR China

ARTICLE INFO

Keywords:
Interpolation-free
Cell-centered discretization
Coercivity

ABSTRACT

We present a novel cell-centered finite volume discretization of the heterogeneous and anisotropic diffusion problems on polygonal meshes. The unknowns of the resulting linear scheme are the values at the cell centers, and no auxiliary unknowns are involved. The usual star-shaped assumption on the mesh is abolished, and we only require that each mesh cell is simply-connected. The new scheme has a small stencil, a nine-point stencil on the structured quadrilateral meshes, and a five-point one on the rectangular meshes if the diffusion coefficient is a scalar function. More important is that the new scheme has the ability to deal with arbitrary discontinuities. The coercivity is proved under a certain assumption. To the best of our knowledge, this is the first linear cell-centered scheme that is interpolation-free and of second order accuracy on arbitrary meshes with arbitrary discontinuities. Numerical experiments show that the new linear finite volume scheme is robust and efficient, and maintains optimal convergence rates for the solution and flux in most extreme cases on general polygonal meshes.

1. Introduction

Consider the following heterogeneous and anisotropic diffusion problem

$$\begin{cases} -\mathrm{div}(\Lambda \nabla u) = f, & in\ \ \Omega, \\ u = g_D, & on\ \Gamma_D, \\ -\Lambda \nabla u \cdot \boldsymbol{n} = g_N, & on\ \Gamma_N, \end{cases} \tag{1}$$

where $\Omega \subset R^2$ is a polygonal domain with the boundary $\partial\Omega = \Gamma_D \cup \Gamma_N$, Λ is a symmetric and positive-definite tensor, and f, g_D, g_N denote the source or sink term, the Dirichlet and the Neumann boundary data, respectively.

Heterogeneous and anisotropic diffusion problems appear in a wide range of applications, such as radiation hydrodynamics [37], Z-pinch related research [15], oil-water displacement simulation [12], ground water simulation [33], and so on. Highly distorted meshes and strongly anisotropic diffusion tensors pose great challenges to the design and theoretical analysis of accurate and effective numerical schemes. In the numerical simulation of diffusion process, finite volume method (FV) has become one of the most commonly used methods because of its simplicity and local conservation.

In recent decades, many authors have conducted extensive research on the development of effective FV schemes. The Hybrid Mimetic Mixed (HHM) schemes, including the hybrid finite volume (HFV) scheme [19], the mixed finite volume (MFV) scheme [17], and the mimetic finite difference (MFD) schemes [8,9,43,36], have both cell-centered unknowns and edge (or edge-flux) unknowns. The DDFV schemes [25,6,44] have cell-centered unknowns and vertex unknowns simultaneously. There exist also FV schemes that have only vertex unknowns [18,53]. For a more comprehensive review of the finite volume schemes, we refer the reader to e.g. [16,42]. In this paper, we mainly focus on the cell-centered finite volume schemes that only define unknowns at the cell centers. In order to improve the accuracy of the cell-centered FV schemes, it is a standard practice to introduce some auxiliary unknowns, which are usually interpolated by the cell-centered ones. According to the use or definition of auxiliary unknowns, cell-centered finite volume schemes can be roughly divided into the following categories.

The well-known multi-point flux approximation scheme (MPFA) [1,2] uses the edge unknowns as auxiliary ones. The edge unknowns, usually defined at the edge midpoints, are eliminated by solving a local

* Corresponding author.
E-mail addresses: miaoshuai18@gscaep.ac.cn (S. Miao), wu_jiming@iapcm.ac.cn (J. Wu), yao_yanzhong@iapcm.ac.cn (Y. Yao).

https://doi.org/10.1016/j.camwa.2022.11.023
Received 31 May 2022; Received in revised form 15 September 2022; Accepted 25 November 2022

system. Follow up development includes MPFA-L [3] and MPFA-G [4], etc. The harmonic averaging point (HAP) is a special point on the edge and the related auxiliary unknown has a simple and elegant two-point interpolation formula. A cell-centered scheme using HAP as the auxiliary unknown was proposed in [5]. Then it was extended to the 3D case [20]. Some other linear and nonlinear cell-centered schemes based on HAP can be found in [30,52,45,23,11]. However, it is possible for HAP to be located outside of the edge, which will cause a possible loss of accuracy and even lead to completely wrong results [46,56,54].

The second category defines the auxiliary unknowns at cell vertices. Typical examples include the nine-point scheme or the diamond scheme [26,13,50,22,10]. There are many papers on the design of interpolation algorithms for the vertex unknowns, see, e.g., [13,22]. These algorithms are either difficult to extend to 3D cases or less accurate in discontinuous cases [34]. In addition, theoretical analysis, especially the coercivity analysis of the nine-point scheme or diamond scheme, is very difficult, and the introduction of auxiliary unknowns makes the problem even more serious [13]. Based on the original idea in [40], nonlinear positive-preserving cell-centered FV schemes were studied [27,55]. In this case, the vertex unknowns are even required to be interpolated as the convex combinations of cell-centered unknowns, which is more difficult than the design of positivity-preserving schemes itself. In order to overcome this difficulty, some positive-preserving cell-centered schemes without interpolation constraints were suggested [51,21,41], but this approach introduces a certain truncation error that is not easy to analyze.

Here we are interested in the third category that does not utilize any auxiliary unknowns. The two-point flux approximation (TPFA) scheme is a typical example. However, if a certain orthogonality condition is not satisfied, the TPFA scheme will produce completely wrong results [1]. In 2009, Lipnikov, Svyatskiy and Vassilevski proposed an interpolation-free monotone scheme [28] for 2D diffusion problems, which is the first interpolation-free nonlinear two-point flux approximation (NTPFA) scheme. Then it was extended to 3D diffusion problem [14] and advection-diffusion equation [29,38]. The relevant nonlinear iterative acceleration algorithms were studied in [31,49]. However, these schemes are nonlinear ones and only allow one discontinuous line per cell. For a more detailed information on the interpolation-free NTPFA, we refer the reader to [47].

There exist some other papers where auxiliary unknowns are not explicitly introduced but a certain interpolation algorithm is still required. For example, inspired by [5] and [48], the authors in [46] split the flux into harmonic and transversal components, and then interpolated the second component by the homogenization function. In order to obtain a positivity-preserving scheme, this approach requires a certain search algorithm and the resulting scheme usually has a large stencil.

In conclusion, most existing linear or nonlinear cell-centered FV schemes have auxiliary unknowns of a certain kind, and the related interpolation and theoretical analysis are two important and difficult issues. In this paper, we use a novel and simple tool to construct a linear cell-centered finite volume scheme without auxiliary unknowns. The main features of the resulting linear cell-centered scheme can be summarized as follows.

- It is interpolation-free and has only cell-centered unknowns.
- It allows arbitrary discontinuities and full diffusion tensors.
- It works on the simply-connected polygonal meshes, including the star-shaped one as a special case.
- It has a small stencil and leads to a nine-point scheme on the structured quadrilateral meshes.
- It has approximately second-order accuracy for L^2 error and first-order accuracy for H^1 error in most extreme cases.

The rest of this paper is organized as follows. In Section 2, we introduce a novel tool and use it to construct an interpolation-free cell-centered scheme for the diffusion equation on polygonal meshes. In Section 3, the coercivity of the scheme is studied. The numerical results are presented in Section 4 to show the performance of the new scheme on some challenging problems. Finally, the results obtained from this paper are summarized in the last section.

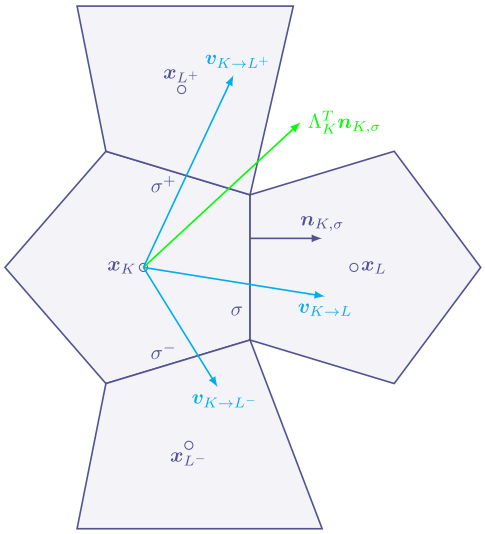

Fig. 1. The stencil of the one-sided flux approximation.

2. An interpolation-free cell-centered discretization

We use the following notations and assumptions throughout this paper.

- $\mathcal{M} = \{K\}$ is the set of non-overlapped open polygonal cells such that $\overline{\Omega} = \bigcup_{K\in\mathcal{M}} \overline{K}$. The measure of the generic cell K is denoted by $|K|$. Let $h = \max_{K\in\mathcal{M}} h_K$ be the mesh size, where h_K is the diameter of K. We assume that K is simply-connected, that is, any two points of $\overline{K}$ can be connected by a continuous, piecewise linear curve inside K.
- $\mathcal{E} = \{\sigma\}$ is the set of disjoint edges in $\overline{\Omega}$. The measure of the generic edge σ is denoted by $|\sigma|$. Let $\mathcal{E}_{int} = \mathcal{E} \cap \Omega$ and $\mathcal{E}_{ext} = \mathcal{E} \cap \partial\Omega$ denote the sets of interior and exterior edges, respectively. We assume that, for all $K \in \mathcal{M}$, there exists a subset $\mathcal{E}_K$ of $\mathcal{E}$ such that $\partial K = \bigcup_{\sigma\in\mathcal{E}_K} \overline{\sigma}$ and the number of edges in $\mathcal{E}_K$ is n_K. For $\sigma \in \mathcal{E}_K$, $\boldsymbol{n}_{K,\sigma}$ denotes the unit vector normal to σ outward to K.
- $\boldsymbol{x}_K \in K$ is the cell center of K (i.e. the average of the cell vertices), and it also represents the position vector of the cell center. The approximation value of the solution u at the cell center $\boldsymbol{x}_K$ is denoted as u_K and Λ_K stands for $\Lambda(\boldsymbol{x}_K)$.
- $\mathcal{H}_\mathcal{M} = \{u_K, K \in \mathcal{M}\}$ is the discrete solution space.
- $\simeq$ is used to indicate that the relevant approximation satisfies the linearity-preserving criterion, that is, when the solution u is piecewise linear and the diffusion tensor is piecewise constant with respect to the mesh, it is an accurate approximation.

2.1. The construction vector

Consider an interior edge σ shared by the two cells K and L, i.e., $\sigma \in \mathcal{E}_K \cap \mathcal{E}_L$, see Fig. 1. Let $\boldsymbol{n}_{K,\sigma}$ (resp. $\boldsymbol{t}_{K,\sigma}$) be the unit normal vector outward to K (resp. tangential vector), satisfying

$$\boldsymbol{t}_{K,\sigma} = -\mathcal{R}\boldsymbol{n}_{K,\sigma}, \quad \mathcal{R} = \begin{pmatrix} 0 & 1 \\ -1 & 0 \end{pmatrix}. \tag{2}$$

Obviously, we have $\boldsymbol{n}_{K,\sigma} = \mathcal{R}\boldsymbol{t}_{K,\sigma}$ and $\mathcal{R}^T = -\mathcal{R}$. Denote $\lambda_{K,\sigma}^{(n)} = \boldsymbol{n}_{K,\sigma}^T \Lambda_K^T \boldsymbol{n}_{K,\sigma}$ and $\lambda_{L,\sigma}^{(n)} = \boldsymbol{n}_{K,\sigma}^T \Lambda_L^T \boldsymbol{n}_{K,\sigma}$. The following new and important

result will play a key role in the construction of the new interpolation-free cell-centered scheme.

Theorem 2.1. *Let σ be an interior edge shared by two simply-connected polygonal cells K and L. Assume that in (1) the solution $u(\boldsymbol{x})$ is piecewise linear and the diffusion tensor Λ is piecewise constant on K and L, respectively. Assume also that $u(\boldsymbol{x})$ and the flux $(-\Lambda\nabla u)\cdot\boldsymbol{n}_{K,\sigma}$ are continuous across σ. Then, we have*

$$u(\boldsymbol{x}_L)-u(\boldsymbol{x}_K)=(\nabla u)|_K\cdot\boldsymbol{v}_{K\to L}, \tag{3}$$

where $(\nabla u)|_K$ is the gradient of $u(\boldsymbol{x})$ on cell K and $\boldsymbol{v}_{K\to L}$ is the so-called construction vector, defined by

$$\boldsymbol{v}_{K\to L}=\boldsymbol{x}_\sigma-\boldsymbol{x}_K+\mathbb{T}_{K\to L}^T(\boldsymbol{x}_L-\boldsymbol{x}_\sigma),\quad \forall\boldsymbol{x}_\sigma\in\overline{\sigma} \tag{4}$$

and

$$\mathbb{T}_{K\to L}=\begin{pmatrix}\boldsymbol{t}_{K,\sigma}^T\\ \boldsymbol{n}_{K,\sigma}^T\Lambda_L\end{pmatrix}^{-1}\begin{pmatrix}\boldsymbol{t}_{K,\sigma}^T\\ \boldsymbol{n}_{K,\sigma}^T\Lambda_K\end{pmatrix}. \tag{5}$$

Proof. To begin with, by the continuity assumption on the solution and the flux, we have

$$\begin{cases}\boldsymbol{t}_{K,\sigma}\cdot(\nabla u)|_K=\boldsymbol{t}_{K,\sigma}\cdot(\nabla u)|_L,\\ \boldsymbol{n}_{K,\sigma}\cdot(-\Lambda\nabla u)|_K=\boldsymbol{n}_{K,\sigma}\cdot(-\Lambda\nabla u)|_L,\end{cases} \tag{6}$$

where the second equation is equivalent to $\left(\Lambda_K^T\boldsymbol{n}_{K,\sigma}\right)\cdot(\nabla u)|_K=\left(\Lambda_L^T\boldsymbol{n}_{K,\sigma}\right)\cdot(\nabla u)|_L$. Here and hereafter, the superscript T is retained for Λ to indicate that the relevant derivation holds also for the case where Λ is asymmetric. The above equations can be rewritten to reach the following matrix form [48,34],

$$(\nabla u)|_L=\mathbb{T}_{K\to L}(\nabla u)|_K, \tag{7}$$

where $\mathbb{T}_{K\to L}$ is a 2×2 matrix, given by (5). Furthermore, for any $\boldsymbol{x}_\sigma\in\overline{\sigma}$, since K is simply-connected, we can always find a piecewise continuous line $\boldsymbol{x}_K=\boldsymbol{x}_0\to\boldsymbol{x}_1\to\boldsymbol{x}_2\to\cdots\to\boldsymbol{x}_n=\boldsymbol{x}_\sigma$, connecting $\boldsymbol{x}_K$ and $\boldsymbol{x}_\sigma$ and located inside K, such that

$$\begin{aligned}u(\boldsymbol{x}_\sigma)-u(\boldsymbol{x}_K)&=\sum_{i=1}^n(u(\boldsymbol{x}_i)-u(\boldsymbol{x}_{i-1}))\\&=\sum_{i=1}^n(\nabla u)|_K\cdot(\boldsymbol{x}_i-\boldsymbol{x}_{i-1})=(\nabla u)|_K\cdot(\boldsymbol{x}_\sigma-\boldsymbol{x}_K),\end{aligned}$$

where we have used the fact that ∇u is constant on K. Analogously,

$$u(\boldsymbol{x}_L)-u(\boldsymbol{x}_\sigma)=(\nabla u)|_L\cdot(\boldsymbol{x}_L-\boldsymbol{x}_\sigma).$$

Adding the above two equations yields

$$u(\boldsymbol{x}_L)-u(\boldsymbol{x}_K)=(\nabla u)|_K\cdot(\boldsymbol{x}_\sigma-\boldsymbol{x}_K)+(\nabla u)|_L\cdot(\boldsymbol{x}_L-\boldsymbol{x}_\sigma).$$

Finally, by (7), we obtain (3) and (4). The proof is complete.

Remark 1. Theorem 2.1 can be easily extended to the case where K and L have no common edges or even no common vertices. This topic is not touched here since the present result is enough for the study of this paper.

Next, we provide some properties of the construction vector $\boldsymbol{v}_{K\to L}$ defined by (4).

Theorem 2.2. *Under the same assumptions of Theorem 2.1, the construction vector defined by (4) is invariant with respect to $\boldsymbol{x}_\sigma$ in the sense that*

$$\begin{aligned}\boldsymbol{v}_{K\to L}&=\boldsymbol{x}_\sigma-\boldsymbol{x}_K+\mathbb{T}_{K\to L}^T(\boldsymbol{x}_L-\boldsymbol{x}_\sigma)\\&=\boldsymbol{x}'_\sigma-\boldsymbol{x}_K+\mathbb{T}_{K\to L}^T(\boldsymbol{x}_L-\boldsymbol{x}'_\sigma),\quad\forall\boldsymbol{x}_\sigma,\boldsymbol{x}'_\sigma\in\overline{\sigma}.\end{aligned} \tag{8}$$

Moreover, we have

$$\boldsymbol{v}_{K\to L}=\boldsymbol{x}_L-\boldsymbol{x}_K+\frac{(\boldsymbol{x}_L-\boldsymbol{x}_\sigma)\cdot\boldsymbol{n}_{K,\sigma}}{\lambda_{L,\sigma}^{(n)}}(\Lambda_K^T-\Lambda_L^T)\boldsymbol{n}_{K,\sigma},\quad\forall\boldsymbol{x}_\sigma\in\overline{\sigma}. \tag{9}$$

Proof. From (5), we see that

$$\begin{pmatrix}\boldsymbol{t}_{K,\sigma}^T\\ \boldsymbol{n}_{K,\sigma}^T\Lambda_L\end{pmatrix}\mathbb{T}_{K\to L}=\begin{pmatrix}\boldsymbol{t}_{K,\sigma}^T\\ \boldsymbol{n}_{K,\sigma}^T\Lambda_K\end{pmatrix},$$

which implies that

$$\mathbb{T}_{K\to L}^T\boldsymbol{t}_{K,\sigma}=\boldsymbol{t}_{K,\sigma}.$$

As a result,

$$\mathbb{T}_{K\to L}^T(\boldsymbol{x}'_\sigma-\boldsymbol{x}_\sigma)=\boldsymbol{x}'_\sigma-\boldsymbol{x}_\sigma,\quad\forall\boldsymbol{x}_\sigma,\boldsymbol{x}'_\sigma\in\overline{\sigma},$$

which leads to (8). By (2) and through some straightforward calculations, we have

$$\begin{pmatrix}\boldsymbol{t}_{K,\sigma}^T\\ \boldsymbol{n}_{K,\sigma}^T\Lambda_L\end{pmatrix}^{-1}=\frac{1}{\lambda_{L,\sigma}^{(n)}}\mathcal{R}(-\Lambda_L^T\boldsymbol{n}_{K,\sigma},\boldsymbol{t}_{K,\sigma}).$$

It follows from (5) that

$$\begin{aligned}\mathbb{T}_{K\to L}&=\begin{pmatrix}\boldsymbol{t}_{K,\sigma}^T\\ \boldsymbol{n}_{K,\sigma}^T\Lambda_L\end{pmatrix}^{-1}\left\{\begin{pmatrix}\boldsymbol{t}_{K,\sigma}^T\\ \boldsymbol{n}_{K,\sigma}^T\Lambda_L\end{pmatrix}+\begin{pmatrix}\boldsymbol{0}^T\\ \boldsymbol{n}_{K,\sigma}^T(\Lambda_K-\Lambda_L)\end{pmatrix}\right\}\\&=\mathbb{I}+\frac{1}{\lambda_{L,\sigma}^{(n)}}\boldsymbol{n}_{K,\sigma}\boldsymbol{n}_{K,\sigma}^T(\Lambda_K-\Lambda_L),\end{aligned} \tag{10}$$

where $\boldsymbol{0}$ stands for a generic zero vector. Inserting (10) into (4), we immediately reach (9) and complete the proof.

Theorem 2.3. *For the construction vector defined by (4), we have*

$$\boldsymbol{v}_{K\to L}+\mathbb{T}_{K\to L}^T\boldsymbol{v}_{L\to K}=\boldsymbol{0}. \tag{11}$$

Proof. By Theorem 2.1, we have

$$u(\boldsymbol{x}_L)-u(\boldsymbol{x}_K)=(\nabla u)|_K\cdot\boldsymbol{v}_{K\to L},\quad u(\boldsymbol{x}_K)-u(\boldsymbol{x}_L)=(\nabla u)|_L\cdot\boldsymbol{v}_{L\to K}.$$

It follows that

$$(\nabla u)|_K\cdot\boldsymbol{v}_{K\to L}+(\nabla u)|_L\cdot\boldsymbol{v}_{L\to K}=0.$$

Substituting (7) into the above equation, we get

$$(\nabla u)|_K\cdot\left(\boldsymbol{v}_{K\to L}+\mathbb{T}_{K\to L}^T\boldsymbol{v}_{L\to K}\right)=0.$$

Note that the above derivation is true when u is any linear function. By choosing $u=x$ and $u=y$, respectively, we reach (11) and complete the proof.

2.2. The one-sided flux

Now, we are ready to describe the construction of the interpolation-free cell-centered scheme, in which the brick is the so-called one-sided flux constructed from the point of K. According to the usual definition [52], the one-sided flux only uses the information on one side of the edge. Here, the one-sided flux uses not only the information of the cell K, but also the information of the cells that share a common edge with K. Moreover, in this subsection, we only consider the Dirichlet boundary conditions to keep the main idea clear. The discussion on the Neumann boundary conditions is moved to subsection 2.5.

For simplicity of exposition, we denote by $\mathcal{M}_K$ the set of cells that have a common edge with K and all possible boundary edges of K. So, when we write $L\in\mathcal{M}_K$, then L is either a co-edge cell of K or

an edge on the domain boundary $\partial\Omega$. We extend the definition of the construction vector to cover all elements of $\mathcal{M}_K$ as follows:

$$\boldsymbol{v}_{K\to L} = \boldsymbol{x}_\sigma - \boldsymbol{x}_K, \quad \forall L = \sigma \in \mathcal{M}_K \cap \partial\Omega, \tag{12}$$

where $\boldsymbol{x}_\sigma$ is the position vector of the midpoint of σ. For $\sigma \in \mathcal{E}_K$, we first decompose the co-normal vector $|\sigma|\Lambda_K^T \boldsymbol{n}_{K,\sigma}$ by the three construction vectors $\boldsymbol{v}_{K\to L^-}$, $\boldsymbol{v}_{K\to L}$ and $\boldsymbol{v}_{K\to L^+}$, see Fig. 1, where $\sigma = \mathcal{E}_K \cap \mathcal{E}_L, \sigma^- = \mathcal{E}_K \cap \mathcal{E}_{L^-}$ and $\sigma^+ = \mathcal{E}_K \cap \mathcal{E}_{L^+}$.

Case I: Any two of $\boldsymbol{v}_{K\to L^-}$, $\boldsymbol{v}_{K\to L}$ and $\boldsymbol{v}_{K\to L^+}$ are not collinear.
In this case, we have

$$|\sigma|\Lambda_K^T \boldsymbol{n}_{K,\sigma} = \alpha_{K,\sigma^-}\boldsymbol{v}_{K\to L^-} + \beta_{K,\sigma^-}\boldsymbol{v}_{K\to L}, \tag{13}$$

where

$$\alpha_{K,\sigma^-} = \frac{|\sigma|\Lambda_K^T \boldsymbol{n}_{K,\sigma}\cdot \mathcal{R}\boldsymbol{v}_{K\to L}}{\boldsymbol{v}_{K\to L^-}\cdot \mathcal{R}\boldsymbol{v}_{K\to L}}, \quad \beta_{K,\sigma^-} = \frac{|\sigma|\Lambda_K^T \boldsymbol{n}_{K,\sigma}\cdot \mathcal{R}\boldsymbol{v}_{K\to L^-}}{\boldsymbol{v}_{K\to L}\cdot \mathcal{R}\boldsymbol{v}_{K\to L^-}}. \tag{14}$$

Analogously,

$$|\sigma|\Lambda_K^T \boldsymbol{n}_{K,\sigma} = \alpha_{K,\sigma^+}\boldsymbol{v}_{K\to L^+} + \beta_{K,\sigma^+}\boldsymbol{v}_{K\to L}, \tag{15}$$

where

$$\alpha_{K,\sigma^+} = \frac{|\sigma|\Lambda_K^T \boldsymbol{n}_{K,\sigma}\cdot \mathcal{R}\boldsymbol{v}_{K\to L}}{\boldsymbol{v}_{K\to L^+}\cdot \mathcal{R}\boldsymbol{v}_{K\to L}}, \quad \beta_{K,\sigma^+} = \frac{|\sigma|\Lambda_K^T \boldsymbol{n}_{K,\sigma}\cdot \mathcal{R}\boldsymbol{v}_{K\to L^+}}{\boldsymbol{v}_{K\to L}\cdot \mathcal{R}\boldsymbol{v}_{K\to L^+}}. \tag{16}$$

Then, from (13) and (15), we have

$$|\sigma|\Lambda_K^T \boldsymbol{n}_{K,\sigma} = \frac{1}{2}\left(\alpha_{K,\sigma^-}\boldsymbol{v}_{K\to L^-} + (\beta_{K,\sigma^-}+\beta_{K,\sigma^+})\boldsymbol{v}_{K\to L} + \alpha_{K,\sigma^+}\boldsymbol{v}_{K\to L^+}\right). \tag{17}$$

Furthermore, by Theorem 2.1 and (17), we deduce that

$$\begin{aligned}\int_\sigma (-\Lambda\nabla u)\cdot \boldsymbol{n}_{K,\sigma}\,\mathrm{d}s &= \int_\sigma -\nabla u\cdot(\Lambda^T \boldsymbol{n}_{K,\sigma})\,\mathrm{d}s\\ &\simeq -(\nabla u)|_K\cdot(|\sigma|\Lambda_K^T \boldsymbol{n}_{K,\sigma})\\ &= \frac{1}{2}(\alpha_{K,\sigma^-}(u(\boldsymbol{x}_K)-u(\boldsymbol{x}_{L^-})) + (\beta_{K,\sigma^-}\\ &\quad + \beta_{K,\sigma^+})(u(\boldsymbol{x}_K)-u(\boldsymbol{x}_L)) + \alpha_{K,\sigma^+}(u(\boldsymbol{x}_K)-u(\boldsymbol{x}_{L^+}))),\end{aligned}$$

which leads to a linearity-preserving one-sided flux, given by

$$\widetilde{F}_{K,\sigma} = \frac{1}{2}\left(\alpha_{K,\sigma^-}(u_K-u_{L^-}) + (\beta_{K,\sigma^-}+\beta_{K,\sigma^+})(u_K-u_L) + \alpha_{K,\sigma^+}(u_K-u_{L^+})\right). \tag{18}$$

Obviously, the above discrete flux has only cell-centered unknowns and the possible Dirichlet boundary data, and it does not involve any auxiliary unknowns.

Case II: $\boldsymbol{v}_{K\to L}$ is collinear with $\boldsymbol{v}_{K\to L^+}$ or $\boldsymbol{v}_{K\to L^-}$.
In this case, the above vector decomposition will fail. Although we have never encountered such an extreme situation in our numerical experiments, we still propose a solution (do not rule out a better way) in case it really happens. For $\sigma \in \mathcal{E}_K$, let

$$\boldsymbol{\zeta}_{K,\sigma} = \left(\cos(\frac{2(j_\sigma-1)\pi}{n_K}),\ \sin(\frac{2(j_\sigma-1)\pi}{n_K})\right)^T, \quad j_\sigma \in \{1,2,\cdots,n_K\}, \tag{19}$$

where j_σ represents the local number of edge σ with respect to cell K. Define

$$\boldsymbol{v}^\varepsilon_{K\to L} = \boldsymbol{v}_{K\to L} + \varepsilon_K\boldsymbol{\zeta}_{K,\sigma}, \quad \forall L \in \mathcal{M}_K, \tag{20}$$

where ε_K is a parameter and in practice, we suggest $\varepsilon_K = O(h_K^3)$.

Theorem 2.4. *For $L, L^- \in \mathcal{M}_K$, assume that K, L and L^- share a common vertex. If $\boldsymbol{v}_{K\to L}$ and $\boldsymbol{v}_{K\to L^-}$ are collinear, then there exists at most one nonzero value for ε_K, such that $\boldsymbol{v}^\varepsilon_{K\to L}$ and $\boldsymbol{v}^\varepsilon_{K\to L^-}$ are also collinear.*

Proof. By the assumption,

$$\begin{aligned}\det(\boldsymbol{v}^\varepsilon_{K\to L}, \boldsymbol{v}^\varepsilon_{K\to L^-}) &= \left(\det(\boldsymbol{v}_{K\to L}, \boldsymbol{\zeta}_{K,\sigma^-}) + \det(\boldsymbol{v}_{K\to L^-}, \boldsymbol{\zeta}_{K,\sigma})\right)\varepsilon_K\\ &\quad + \det(\boldsymbol{\zeta}_{K,\sigma}, \boldsymbol{\zeta}_{K,\sigma^-})\varepsilon_K^2.\end{aligned}$$

From the definition of $\boldsymbol{\zeta}_{K,\sigma}$ in (19), we see that $\boldsymbol{\zeta}_{K,\sigma}$ and $\boldsymbol{\zeta}_{K,\sigma^-}$ are not collinear so that $\det(\boldsymbol{\zeta}_{K,\sigma}, \boldsymbol{\zeta}_{K,\sigma^-}) \neq 0$. Then there exists at most one nonzero value for ε_K, such that

$$\det(\boldsymbol{v}^\varepsilon_{K\to L}, \boldsymbol{v}^\varepsilon_{K\to L^-}) = 0.$$

The proof is complete.

Theorem 2.4 implies that if the construction vectors $\boldsymbol{v}_{K\to L}$ and $\boldsymbol{v}_{K\to L^-}$ are collinear, we can always find one ε_K, such that $\boldsymbol{v}^\varepsilon_{K\to L}$ and $\boldsymbol{v}^\varepsilon_{K\to L^-}$ are not collinear. Replacing $\boldsymbol{v}_{K\to L}$, $\boldsymbol{v}_{K\to L^-}$ and $\boldsymbol{v}_{K\to L^+}$ with $\boldsymbol{v}^\varepsilon_{K\to L}$, $\boldsymbol{v}^\varepsilon_{K\to L^-}$ and $\boldsymbol{v}^\varepsilon_{K\to L^+}$ respectively, we can still obtain the one-sided flux in the form of (18). Here, we remark that, in this case, the counterpart of (18) is no longer linearity-preserving, but the optimal convergence rate is still maintained. This trick should be used in the Case I if the vectors are "nearly" (but not) collinear, for numerical stability.

2.3. A unique definition of edge flux

Based on the one-sided fluxes, we define a unique flux approximation for each edge. Specifically, for $\sigma \in \mathcal{E}_K$, we define

$$F_{K,\sigma} = \begin{cases}\mu_{K,\sigma}\widetilde{F}_{K,\sigma} - \mu_{L,\sigma}\widetilde{F}_{L,\sigma}, & \sigma \in \mathcal{E}_K \cap \mathcal{E}_L,\\ \mu_{K,\sigma}\widetilde{F}_{K,\sigma}, & \sigma \in \mathcal{E}_K \cap \mathcal{E}_{ext},\end{cases} \tag{21}$$

where $\mu_{K,\sigma}$ and $\mu_{L,\sigma}$ are two positive parameters, satisfying

$$\mu_{K,\sigma} + \mu_{L,\sigma} = 1, \quad \sigma \in \mathcal{E}_K \cap \mathcal{E}_L; \quad \mu_{K,\sigma} = 1, \quad \sigma \in \mathcal{E}_K \cap \mathcal{E}_{ext}. \tag{22}$$

There are many choices for $\mu_{K,\sigma}$ and $\mu_{L,\sigma}$ when σ is an interior edge. In this paper, we choose

$$\mu_{K,\sigma} = \mu_{L,\sigma} = 0.5.$$

Obviously, we have the following local conservation

$$F_{K,\sigma} + F_{L,\sigma} = 0, \quad \forall \sigma \in \mathcal{E}_K \cap \mathcal{E}_L. \tag{23}$$

2.4. The finite volume equation

The interpolation-free cell-centered discretization (ICD) scheme for (1) can be formulated as: Find $u_K \in \mathcal{H}_\mathcal{M}$, such that

$$\sum_{\sigma\in\mathcal{E}_K\setminus\Gamma_N} F_{K,\sigma} = f_K|K| - \int_{\mathcal{E}_K\cap\Gamma_N} g_N\,ds, \quad \forall K \in \mathcal{M}, \tag{24}$$

where $F_{K,\sigma}$ is given by (21) and f_K denotes the mean value of f on the cell K.

On the structured quadrilateral meshes, the stencils of the one-sided flux $\widetilde{F}_{K,\sigma}$ defined by (18), the final flux approximation $F_{K,\sigma}$ defined by (21) and the FV equation (24) are shown in Fig. 2, respectively, where one can see that the ICD scheme has a nine-point stencil. On the rectangular meshes, if the diffusion coefficient is a scalar function, the new scheme will have a standard five point stencil since the flux $F_{K,\sigma}$ reduces to a two-point approximation. It is interesting to note that, on the triangular meshes, the stencil of the ICD scheme is even smaller than that of the nine-point or diamond scheme (e.g. LPeLSW in [34]), which is shown by Fig. 3.

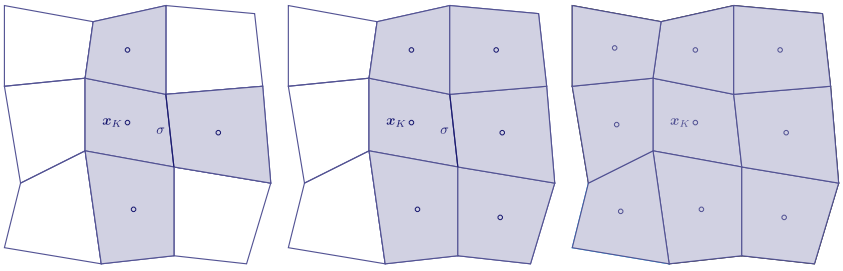

(a) The stencil of $\widetilde{F}_{K,\sigma}$ (b) The stencil of $F_{K,\sigma}$ (c) The stencil of the FV equation

Fig. 2. The relevant stencils in the ICD scheme on the structured quadrilateral meshes.

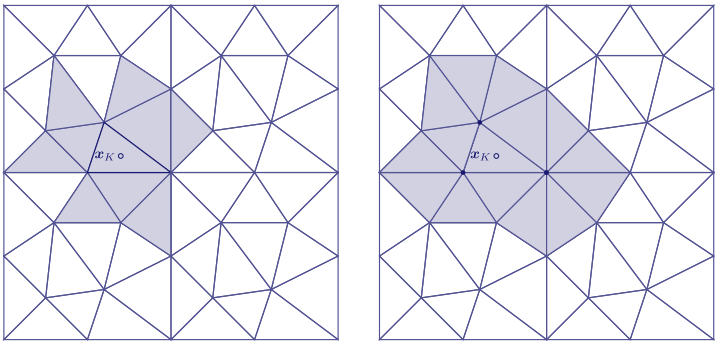

(a) ICD (b) LPeLSW in [34]

Fig. 3. The stencils of two cell-centered schemes on the triangular meshes.

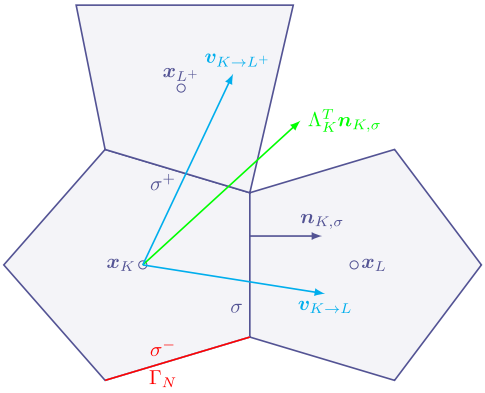

Fig. 4. The configuration of the one-sided flux approximation near the Neumann boundary.

2.5. Neumann boundary conditions

In this subsection, we consider the case where σ or one of its two adjacent edges is located on the Neumann boundary Γ_N. If $\sigma \in \mathcal{E}_K \cap \Gamma_N$, then

$$\widetilde{F}_{K,\sigma} = \int_\sigma -\Lambda \nabla u \cdot \boldsymbol{n}\, \mathrm{d}s = \int_\sigma g_N\, \mathrm{d}s. \tag{25}$$

In addition, without losing generality, assume that $\sigma^- \in \Gamma_N$, see Fig. 4. Then we simply use the two construction vectors $v_{K\to L^+}$ and $v_{K\to L}$ to decompose the co-normal to get (15). Similar to the derivation of (18), we obtain the following one-sided flux

$$\widetilde{F}_{K,\sigma} = \alpha_{K,\sigma^+}(u_K - u_{L^+}) + \beta_{K,\sigma^+}(u_K - u_L). \tag{26}$$

3. Coercivity analysis of the ICD scheme

In this section, we only consider the problem (1) with a full Dirichlet boundary condition, i.e., $\Gamma_N = \emptyset$. For simplicity of exposition, we introduce the following two vectors

$$\delta \mathbf{U}_K = (u_K - u_L, L \in \mathcal{M}_K)^T, \quad \mathbf{F}_K = (\widetilde{F}_{K,\sigma}, \sigma \in \mathcal{E}_K)^T,$$

where $\widetilde{F}_{K,\sigma}$ is defined in (18). Here we require that entries of the above two vectors should be ordered in such a way that $\sigma \in \mathcal{E}_K \cap \mathcal{E}_L$ if σ is an interior edge. Moreover, when $\sigma \in \mathcal{E}_K \cap \mathcal{E}_{ext}$, we assume that $u_L = u_\sigma$. From (18), we see that the ICD scheme has the following local relation

$$\mathbf{F}_K = \mathbb{A}_K \delta \mathbf{U}_K, \quad \forall K \in \mathcal{M}, \tag{27}$$

where $\mathbb{A}_K$ is the so-called cell matrix. Introduce the following diagonal matrix

$$\mathbb{W}_K = diag(\mu_{K,\sigma}, \sigma \in \mathcal{E}_K), \tag{28}$$

where $\mu_{K,\sigma}$ is defined in (22). Denote by ϱ_K the minimum eigenvalue of the symmetric part of matrix $\mathbb{W}_K \mathbb{A}_K$, i.e.

$$\boldsymbol{v}^T \mathbb{W}_K \mathbb{A}_K \boldsymbol{v} = \frac{1}{2} \boldsymbol{v}^T \left(\mathbb{W}_K \mathbb{A}_K + \mathbb{A}_K^T \mathbb{W}_K^T \right) \boldsymbol{v} \geq \varrho_K \|\boldsymbol{v}\|^2, \quad \forall \boldsymbol{v} \in \mathbb{R}^{n_K}, \quad \forall K \in \mathcal{M}. \tag{29}$$

Define

$$\varrho_\sigma = \begin{cases} \frac{1}{2}(\varrho_K + \varrho_L), & \sigma \in \mathcal{E}_K \cap \mathcal{E}_L, \\ \varrho_K, & \sigma \in \mathcal{E}_K \cap \mathcal{E}_{ext}. \end{cases} \tag{30}$$

We introduce the following assumption:

(A1) There exists a positive constant ϱ, independent of h, such that

$\varrho_\sigma \geq \varrho, \quad \forall \sigma \in \mathcal{E}$.

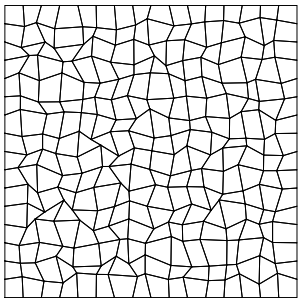

(a) Mesh 1: Random mesh

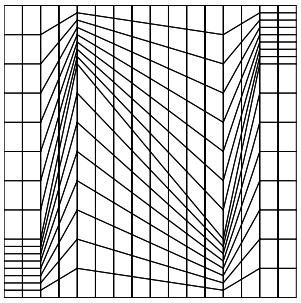

(b) Mesh 2: Kershaw mesh

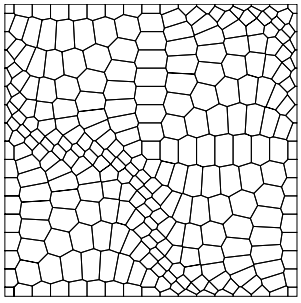

(c) Mesh 3: Polygonal mesh

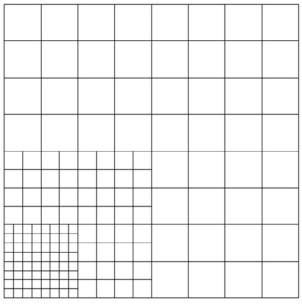

(d) Mesh 4: Locally refined mesh

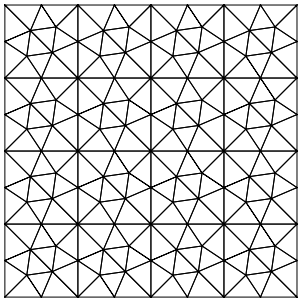

(e) Mesh 5: Triangular mesh

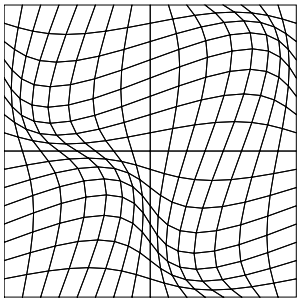

(f) Mesh 6: Sine mesh

Fig. 5. Mesh types used in the numerical tests (Mesh level = 2).

Theorem 3.1. *(Coercivity) Assume that $\Gamma_N = \emptyset$ and the Dirichlet boundary condition of (1) is homogeneous, i.e., $g = 0$. Then, under the assumption (**A**1), we have*

$$\sum_{K\in\mathcal{M}}\sum_{\sigma\in\mathcal{E}_K} u_K F_{K,\sigma} \geq \varrho |u_h|_{1,h}^2, \quad \forall u_h \in \mathcal{H}_{\mathcal{M}}, \tag{31}$$

where the discrete H^1 semi-norm is defined by

$$|u_h|_{1,h} = \left(\sum_{K\in\mathcal{M}} \|\delta \mathbf{U}_K\|^2\right)^{1/2}.$$

Proof. Note that

$$F_{K,\sigma} + F_{L,\sigma} = 0, \quad \sigma \in \mathcal{E}_K \cap \mathcal{E}_L; \quad u_L = u_\sigma = 0, \quad \sigma \in \mathcal{E}_K \cap \mathcal{E}_{ext}.$$

From (21) and (22), we have

$$\begin{aligned}
\sum_{K\in\mathcal{M}}\sum_{\sigma\in\mathcal{E}_K} u_K F_{K,\sigma} &= \sum_{\sigma\in\mathcal{E}_{int}} (u_K - u_L)F_{K,\sigma} + \sum_{\sigma\in\mathcal{E}_{ext}} (u_K - u_\sigma)F_{K,\sigma} \\
&= \sum_{\sigma\in\mathcal{E}_{int}} (u_K - u_L)(\mu_{K,\sigma}\widetilde{F}_{K,\sigma} - \mu_{L,\sigma}\widetilde{F}_{L,\sigma}) \\
&\quad + \sum_{\sigma\in\mathcal{E}_{ext}} (u_K - u_\sigma)\mu_{K,\sigma}\widetilde{F}_{K,\sigma} \\
&= \sum_{K\in\mathcal{M}} (\delta\mathbf{U}_K)^T \mathbb{W}_K \mathbf{F}_K \\
&= \sum_{K\in\mathcal{M}} (\delta\mathbf{U}_K)^T \mathbb{W}_K \mathbb{A}_K \delta\mathbf{U}_K \\
&\geq \sum_{K\in\mathcal{M}} \varrho_K \|\delta\mathbf{U}_K\|^2 \\
&= \sum_{\sigma\in\mathcal{E}_{int}} (\varrho_K + \varrho_L)(u_K - u_L)^2 + \sum_{\sigma\in\mathcal{E}_{ext}} \varrho_K (u_K - u_\sigma)^2 \\
&\geq (\min_{\sigma\in\mathcal{E}} \varrho_\sigma)|u_h|_{1,h}^2,
\end{aligned}$$

which leads to (31) by recalling assumption (**A**1).

The above theorem implies that the coercivity of the ICD scheme depends on the spectral result of the matrix $\mathbb{W}_K\mathbb{A}_K$, which involves

Table 1
Numerical results for Example 4.1.

	Mesh level	1	2	3	4	5
Mesh 4	E_u	4.14×10^{-15}	1.93×10^{-14}	1.67×10^{-14}	5.24×10^{-14}	3.17×10^{-13}
	E_q	6.43×10^{-14}	6.77×10^{-14}	4.61×10^{-13}	1.53×10^{-12}	5.63×10^{-12}
Mesh 5	E_u	7.45×10^{-15}	1.49×10^{-14}	3.33×10^{-14}	6.47×10^{-14}	2.91×10^{-13}
	E_q	7.97×10^{-14}	2.24×10^{-13}	5.81×10^{-13}	1.58×10^{-12}	3.59×10^{-12}
Mesh 6	E_u	4.97×10^{-15}	1.23×10^{-14}	4.09×10^{-14}	1.52×10^{-13}	2.17×10^{-12}
	E_q	7.64×10^{-14}	2.45×10^{-13}	9.36×10^{-13}	3.93×10^{-12}	4.18×10^{-11}

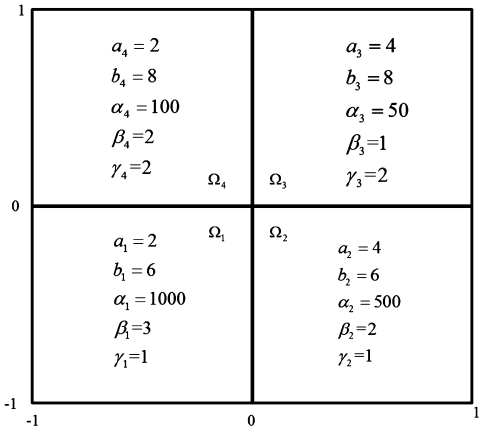

Fig. 6. Coefficients in the definition of diffusion tensor.

Table 2
Comparison of the stencils on Mesh 5.

	Mesh level	1	2	3	4	5
Averaging stencil	ICD	8.57	9.28	9.64	9.82	9.91
	LPeLSW in [34]	9.71	11.39	12.37	12.89	13.15

only local calculations. Thanks to the result of this theorem, (31) can be examined before the solution of (24).

Remark 2. Based on the above coercivity result, a first-order error estimate in the discrete H^1 norm can be obtained through a discrete functional approach, see, e.g. section 4 in [52], which is omitted here.

Remark 3. The ICD scheme proposed in this paper is a linear one, so it cannot be unconditionally positivity-preserving or extremum-preserving. In the applications where the solution bounds are required to maintain, a second-order correction technique is available for the new scheme to reach a nonlinear positivity-preserving or extremum-preserving counterpart. The implementation of such a correction is quite easy and simple. This topic will not be discussed here and we refer the readers to [39,34] for details.

4. Numerical experiments

In this section, we give some numerical examples to investigate the performance of the ICD scheme on a number of distorted polygonal meshes, see Fig. 5. For the need of comparison, the results of the scheme LPeLSW in [34] are sometimes presented. The quantities examined in the numerical tests include the discrete L^2 errors, the discrete H^1 errors and the numerical coercivity. The discrete L^2 and H^1 norms of errors are defined as follows:

$$E_u=\left(\sum_{K\in\mathcal{M}}|K|e_K^2\right)^{1/2},\quad E_q=\left(\sum_{K\in\mathcal{M}}\sum_{L\in\mathcal{M}_K}(e_K-e_L)^2\right)^{1/2},$$

where $e_K=u(\boldsymbol{x}_K)-u_K$. The rate of convergence $R_\alpha(\alpha=u,q)$ is computed by the following formula

$$R_\alpha=\frac{log[E_\alpha(h_2)/E_\alpha(h_1)]}{log(h_2/h_1)},$$

where h_1 and h_2 denote the mesh sizes of two successive mesh levels. In order to investigate the coercivity of the scheme numerically and examine the assumption (**A1**), we introduce the following parameters

$$Coer=\frac{\sum_{\sigma\in\mathcal{E}}F_{K,\sigma}(u_K-u_L)}{\sum_{\sigma\in\mathcal{E}}\frac{|\sigma|}{d_\sigma}(u_K-u_L)^2},\quad \varrho=\min_{\sigma\in\mathcal{E}}\varrho_\sigma,$$

where ϱ_σ is defined in (30), $d_\sigma=d_{K,\sigma}+d_{L,\sigma}$, and $d_{K,\sigma}$ and $d_{L,\sigma}$ denote the orthogonal distances from the relevant cell centers to edge σ. Obviously, the positivity of ϱ implies the effectiveness of assumption (**A1**). We mention that the definition of $Coer$ can be found in, e.g. [42]. In addition, BICGSTAB is used to solve the relevant linear systems with stopping tolerance $\epsilon_{lin}=10^{-15}$.

4.1. Linearity preservation

First, the linearity-preserving property of the new scheme is examined. In this test, the domain $\Omega=[-1,1]\times[-1,1]$ is split into four subdomains $\Omega=\cup_{i=1}^4\Omega_i$, see Fig. 6, and the Dirichlet boundary condition is imposed on $\partial\Omega$ in this test. The diffusion tensor and exact solution are given by

$$\Lambda=\begin{pmatrix}\alpha_i & \gamma_i\\ \gamma_i & \beta_i\end{pmatrix},\quad u(x,y)=a_ix+b_iy+6,\ \text{for}\ (x,y)\in\Omega_i,$$

respectively, where the values of coefficients α_i, β_i, γ_i, a_i and b_i can be found in Fig. 6. Note that the diffusion tensor Λ is discontinuous across the lines $x=0$ and $y=0$. We use Mesh 4, Mesh 5 and Mesh 6 shown in Fig. 5 to test this problem. The numerical results are given in Table 1, where one can see that the ICD scheme reproduces the exact solution. Table 2 shows the averaging stencils of ICD and LPeLSW on each mesh level of Mesh 5. The averaging stencil is the ratio between non-zero entries of the matrix and the total number of rows. We see that the ICD scheme has a smaller stencil on triangular meshes than that of the diamond schemes such as LPeLSW.

4.2. Mild anisotropy

The second test is a little modification of Test 1.2 in the FVCA5 benchmarks [24]. Here we consider the problem (1) on $\Omega=[0,1]\times[0,1]$ with a mild anisotropic tensor

$$\Lambda=\begin{pmatrix}1.5 & 0.5\\ 0.5 & 1.5\end{pmatrix}.$$

The exact solution is

$$u(x,y)=\frac{1}{2}\left[\frac{\sin((1-x)(1-y))}{\sin 1}+(1-x)^3(1-y)^2\right]$$

and a full Dirichlet boundary condition is set on the boundary. We solve this problem on the six mesh types shown in Fig. 5. In particular, Mesh 1 is constructed from the uniform square mesh with mesh size h by a random distortion of the interior vertices

Table 3
Numerical results for Example 4.2 on Mesh 1 to Mesh 6.

	Mesh level	1	2	3	4	5
Mesh 1	E_u	2.68×10^{-3}	6.79×10^{-4}	1.67×10^{-4}	4.71×10^{-5}	1.15×10^{-5}
	R_u		1.92	2.20	1.91	2.03
	E_q	2.82×10^{-2}	1.46×10^{-2}	7.08×10^{-3}	3.47×10^{-3}	1.80×10^{-3}
	R_q		0.92	1.13	1.08	0.94
	ϱ	1.78×10^{-1}	1.09×10^{-1}	9.29×10^{-2}	6.54×10^{-2}	1.97×10^{-2}
	Coer	1.78	1.74	1.74	1.75	1.75
Mesh 2	E_u	5.30×10^{-3}	1.29×10^{-3}	3.23×10^{-4}	8.32×10^{-5}	2.11×10^{-5}
	R_u		2.36	2.13	2.02	2.01
	E_q	7.67×10^{-2}	2.85×10^{-2}	1.06×10^{-2}	3.79×10^{-3}	1.31×10^{-3}
	R_q		1.65	1.52	1.54	1.55
	ϱ	-9.29×10^{-3}	1.99×10^{-2}	1.60×10^{-2}	1.39×10^{-2}	1.27×10^{-2}
	Coer	1.02	0.97	0.94	0.93	0.92
Mesh 3	E_u	2.23×10^{-3}	7.20×10^{-4}	2.09×10^{-4}	5.72×10^{-5}	1.48×10^{-5}
	R_u		1.71	1.81	1.87	1.95
	E_q	2.41×10^{-2}	1.56×10^{-2}	6.37×10^{-3}	2.42×10^{-3}	8.84×10^{-4}
	R_q		0.66	1.31	1.40	1.46
	ϱ	5.63×10^{-3}	-5.98×10^{-3}	-3.84×10^{-3}	-2.31×10^{-2}	-3.09×10^{-2}
	Coer	1.86	1.88	1.90	1.91	1.92
Mesh 4	E_u	5.19×10^{-3}	1.21×10^{-3}	2.89×10^{-4}	7.04×10^{-5}	1.73×10^{-5}
	R_u		2.10	2.07	2.04	2.02
	E_q	3.14×10^{-2}	1.06×10^{-2}	3.58×10^{-3}	1.23×10^{-3}	4.29×10^{-4}
	R_q		1.57	1.56	1.54	1.52
	ϱ	1.98×10^{-1}	1.98×10^{-1}	1.98×10^{-1}	1.98×10^{-1}	1.98×10^{-1}
	Coer	1.90	1.91	1.91	1.92	1.92
Mesh 5	E_u	2.53×10^{-3}	6.50×10^{-4}	1.65×10^{-4}	4.14×10^{-5}	1.04×10^{-5}
	R_u		1.96	1.98	1.99	2.00
	E_q	2.04×10^{-2}	8.84×10^{-3}	4.07×10^{-3}	1.94×10^{-3}	9.49×10^{-4}
	R_q		1.21	1.12	1.07	1.03
	ϱ	7.20×10^{-1}	7.20×10^{-1}	7.20×10^{-1}	7.20×10^{-1}	7.20×10^{-1}
	Coer	1.94	1.96	1.97	1.97	1.97
Mesh 6	E_u	3.84×10^{-3}	1.03×10^{-3}	2.63×10^{-4}	6.60×10^{-5}	1.65×10^{-5}
	R_u		1.98	1.99	2.00	2.00
	E_q	3.27×10^{-2}	1.18×10^{-2}	4.07×10^{-3}	1.39×10^{-3}	4.82×10^{-4}
	R_q		1.53	1.56	1.55	1.53
	ϱ	2.23×10^{-1}	1.74×10^{-1}	1.59×10^{-1}	1.55×10^{-1}	1.54×10^{-1}
	Coer	1.53	1.48	1.46	1.46	1.46

Table 4
Error comparison for Example 4.2 before and after disturbance of the construction vectors.

	Mesh level	1	2	3	4	5
ICD	E_u	3.29×10^{-3}	7.43×10^{-4}	1.89×10^{-4}	5.06×10^{-5}	1.35×10^{-5}
	R_u		2.07	2.19	2.02	1.89
	E_q	3.83×10^{-2}	2.10×10^{-2}	1.02×10^{-2}	5.00×10^{-3}	2.72×10^{-3}
	R_q		0.84	1.56	1.09	0.87
ICD(ϵ)	E_u	7.25×10^{-3}	8.08×10^{-4}	2.11×10^{-4}	5.46×10^{-5}	1.35×10^{-5}
	R_u		3.05	2.15	2.06	2.01
	E_q	1.04×10^{-1}	2.58×10^{-2}	1.17×10^{-2}	5.19×10^{-3}	2.74×10^{-3}
	R_q		1.94	1.27	1.24	0.92

$$x := x + \alpha\xi_x h, \qquad y := y + \alpha\xi_y h. \tag{32}$$

Here ξ_x and ξ_y are random variables belonging to $[-1,1]$ and $\alpha \in [0, 0.5]$ is the degree of distortion. In this test we choose $\alpha = 0.35$.

The convergence rates for the discrete L^2-norm and H^1-norm of the solution errors are graphically depicted in Fig. 7. One can see that the ICD scheme converges with a second order accuracy for the L^2-norm and higher than first order accuracy for the H^1-norm of the solution errors. Numerical results on six mesh types are presented in Table 3, respectively. We observe that the coercivity parameters *Coer* are positive which indicates that the new scheme is coercive in these cases. Moreover, it can be see that the values of ϱ are positive for all six mesh types except the first level of Mesh 2 and the last four levels of Mesh 3. There is no contradiction since assumption (**A**1) is just a sufficient condition for the coercivity result.

Although the collinearity of $\boldsymbol{v}_{K\to L}$ and $\boldsymbol{v}_{K\to L^\pm}$ has never appeared in our numerical experiments, it is still possible, at least it seems so theoretically. Here we investigate the influence of the technique in Case II of subsection 2.2 on the accuracy. We choose

$$\boldsymbol{v}^{\epsilon}_{K\to L} = \boldsymbol{v}_{K\to L} + \gamma_K h_K^3 \boldsymbol{\zeta}_{K,\sigma}, \quad \forall L \in \mathcal{M}_K,$$

where $\gamma_K \in (-1,1)$ is a random number. We use Mesh 1 and set the distortion parameter $\alpha = 0.5$, see Fig. 8. The results are presented in Table 4 where one can see that the optimal convergence rates are still maintained.

4.3. Discontinuous anisotropy

In this test, the domain $\Omega = [0,1]\times[0,1]$ is split into four subdomains $\Omega = \cup_{i=1}^4 \Omega_i$, see Fig. 9, and the homogeneous Dirichlet boundary condi-

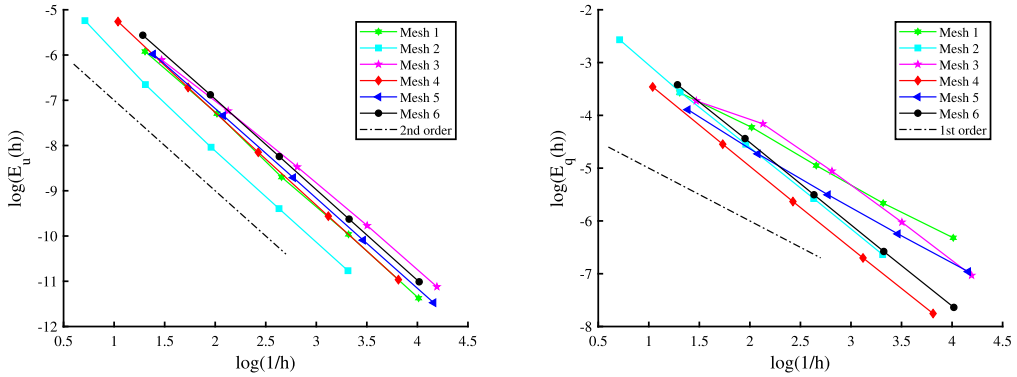

(a) L^2 errors (b) H^1 errors

Fig. 7. L^2 and H^1 errors versus mesh size h for Example 4.2.

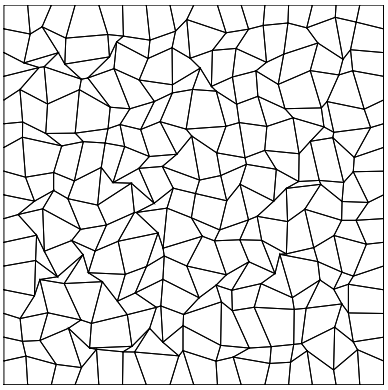

Fig. 8. The random mesh with distortion parameter $\alpha = 0.5$.

$a_4 = 20$ $b_4 = 5$ $c_4 = 0.01$	$a_3 = 0.01$ $b_3 = 10$ $c_3 = 20$
$a_1 = 0.2$ $b_1 = 0.01$ $c_1 = 5$	$a_2 = 0.1$ $b_2 = 20$ $c_2 = 10$

Fig. 9. Coefficients in the definition of diffusion tensor for Example 4.3.

Table 5
Numerical results for Example 4.3.

	Mesh level	1	2	3	4	5
Mesh 4	E_u	1.79×10^{0}	5.25×10^{-1}	1.70×10^{-1}	5.54×10^{-2}	1.60×10^{-2}
	R_u		1.77	1.62	1.62	1.79
	E_q	15.57×10^{0}	7.09×10^{0}	3.62×10^{0}	1.75×10^{0}	6.80×10^{-1}
	R_q		1.13	0.97	1.05	1.36
	ρ	-3.09×10^{-2}	-3.09×10^{-2}	-3.09×10^{-2}	-3.09×10^{-2}	-3.09×10^{-2}
	Coer	6.13	6.02	5.89	5.82	5.78
Mesh 5	E_u	1.67×10^{0}	3.14×10^{-1}	9.10×10^{-2}	1.95×10^{-2}	4.16×10^{-3}
	R_u		2.41	1.79	2.22	2.23
	E_q	2.42×10^{1}	6.10×10^{0}	3.44×10^{0}	1.45×10^{0}	5.99×10^{-1}
	R_q		1.99	0.83	1.25	1.28
	ρ	-2.61×10^{0}	-4.47×10^{0}	-4.47×10^{0}	-2.61×10^{0}	-4.47×10^{0}
	Coer	4.68	5.69	5.73	5.74	5.73
Mesh 6	E_u	1.03×10^{0}	3.06×10^{-1}	9.04×10^{-2}	2.45×10^{-2}	6.28×10^{-3}
	R_u		1.84	1.78	1.89	1.96
	E_q	1.22×10^{1}	4.79×10^{0}	1.68×10^{0}	4.85×10^{-1}	1.28×10^{-1}
	R_q		1.41	1.53	1.80	1.93
	ρ	-1.59×10^{-1}	-4.73×10^{-2}	-7.62×10^{-3}	-2.23×10^{-4}	1.28×10^{-3}
	Coer	6.37	6.07	5.84	5.74	5.69

Table 6
Numerical results for Example 4.4 on Mesh 1.

Mesh level	1	2	3	4	5
E_u	2.26×10^{-2}	6.83×10^{-3}	2.26×10^{-3}	5.99×10^{-4}	1.72×10^{-4}
R_u		1.67	1.74	2.00	1.79
E_q	3.14×10^{-1}	1.54×10^{-1}	6.98×10^{-2}	3.59×10^{-2}	1.75×10^{-2}
R_q		1.00	1.24	1.00	1.03
ρ	-5.23×10^{-2}	-6.13×10^{-2}	-6.29×10^{-2}	-8.50×10^{-2}	-8.41×10^{-2}
Coer	0.49	0.49	0.49	0.48	0.48

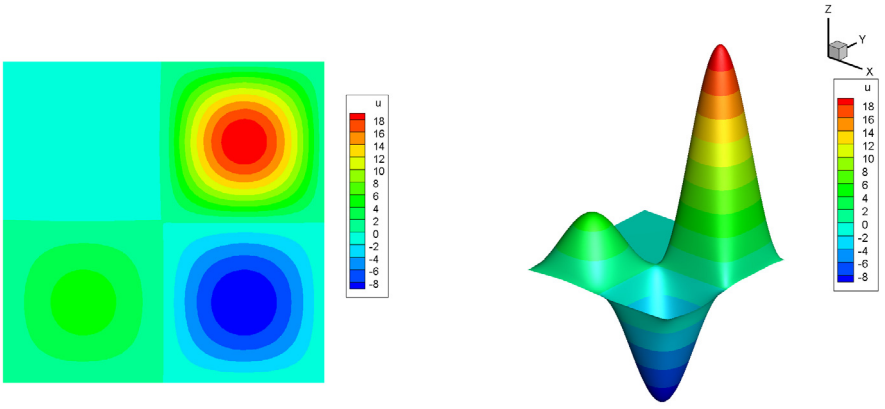

(a) Vertical view (b) Stereogram

Fig. 10. Graphics of the numerical solution for Example 4.3 on level 4 of Mesh 6.

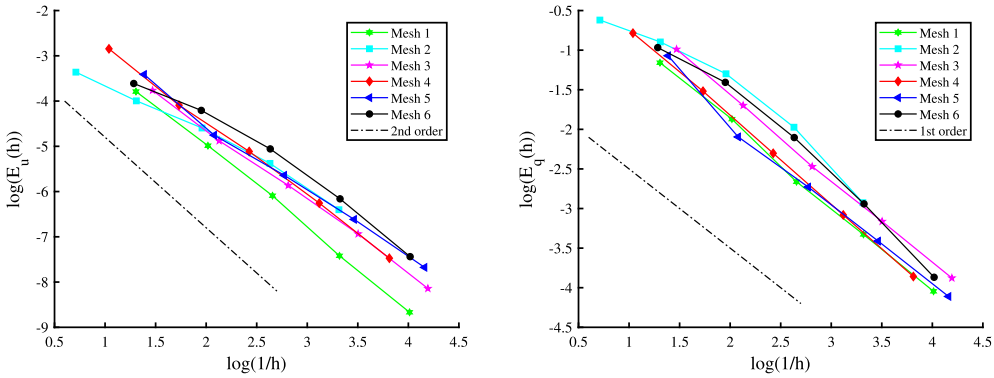

(a) L^2 errors (b) H^1 errors

Fig. 11. L^2 and H^1 errors versus mesh size h for Example 4.4 on Mesh 1 to Mesh 6.

Table 7
Numerical results for Example 4.5 on Mesh 5.

	Mesh level	1	2	3	4	5
ICD	E_u	7.80×10^{-2}	2.11×10^{-2}	3.65×10^{-3}	6.81×10^{-4}	1.50×10^{-4}
	R_u		1.88	2.53	2.42	2.18
	E_q	1.08×10^{0}	3.71×10^{-1}	1.40×10^{-1}	5.36×10^{-2}	2.35×10^{-2}
	R_q		1.54	1.40	1.39	1.19
LPeLSW in [34]	E_u	1.30×10^{-1}	3.68×10^{-2}	7.87×10^{-3}	1.70×10^{-3}	3.99×10^{-4}
	R_u		1.82	2.22	2.21	2.10
	E_q	1.24×10^{0}	5.52×10^{-1}	2.27×10^{-1}	8.71×10^{-2}	3.65×10^{-2}
	R_q		1.16	1.28	1.38	1.25

tion is adopted in this test. The diffusion tensor and exact solution are given by

$$\Lambda = \begin{pmatrix} a_i & 0 \\ 0 & b_i \end{pmatrix}, \quad u(x,y) = c_i \sin(2\pi x)\sin(2\pi y), \text{ for } (x,y) \in \Omega_i,$$

respectively, where the values of coefficients a_i, b_i and c_i are shown in Fig. 9. The diffusion tensor Λ is discontinuous across the lines $x = 1/2$ and $y = 1/2$. Since the gradient of the exact solution is discontinuous at $x = 1/2$ and $y = 1/2$, the solution $u(x, y)$ only belongs to $C^0(\Omega)$.

This problem is solved on Mesh 4, Mesh 5 and Mesh 6, respectively. The relevant numerical results are given in Table 5, where one can see that ICD achieves optimal convergence rates approximately. However, assumption (**A1**) is validated only on the last level of Mesh 6. The graphics of the numerical solution on the fourth level of Mesh 6 are given in Fig. 10.

4.4. Strong anisotropy

We consider the rotating anisotropic diffusion problem from [40, 24], which has proved to be a challenging example by many authors, e.g. [41,46]. We set a full Dirichlet boundary condition on the boundary of the domain $\Omega = [0, 1] \times [0, 1]$. The diffusion tensor is

$$\Lambda(x,y) = \frac{1}{x^2+y^2}\begin{pmatrix} \beta x^2 + y^2 & (\beta-1)xy \\ (\beta-1)xy & x^2 + \beta y^2 \end{pmatrix},$$

where $\beta = 1.0 \times 10^{-3}$. The exact solution is $u(x, y) = \sin(\pi x)\sin(\pi y)$. In this test, the diffusion coefficient used in the discrete flux (21), including the definition of construction vectors and the split of conormals, is determined in the following way

$$\Lambda_{K,\sigma} = \lim_{\substack{\boldsymbol{x}\to\boldsymbol{x}_\sigma \\ \boldsymbol{x}\in K}} \Lambda(\boldsymbol{x}),$$

where $\boldsymbol{x}_\sigma$ is the midpoint of σ.

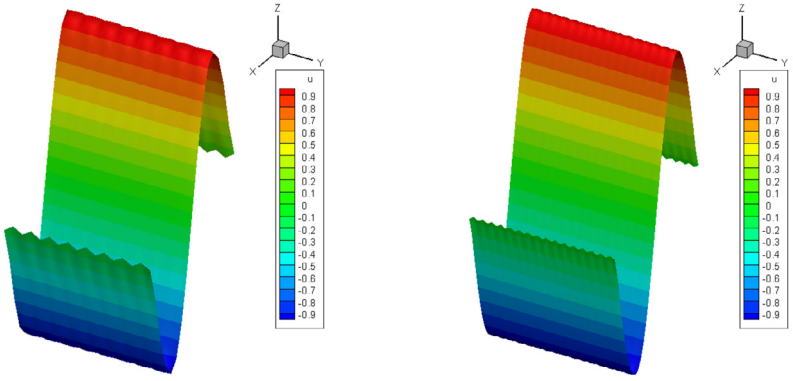

(a) Mesh level=3 (b) Mesh level=4

Fig. 12. The profiles of the numerical solutions by ICD for Example 4.5 on Mesh 5.

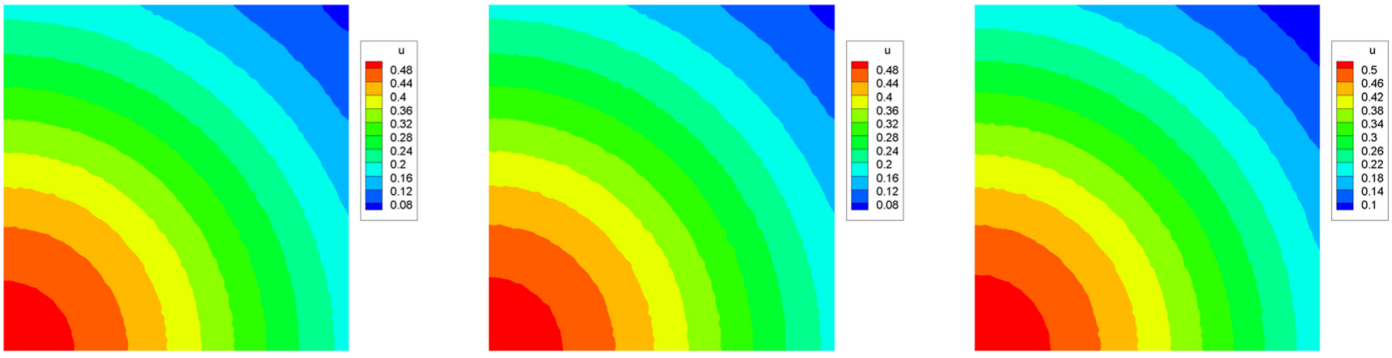

(a) $T = 0.001$ (b) $T = 0.01$ (c) $T = 0.1$

Fig. 13. Solution contours for Example 4.6 on Mesh 1 (Mesh level = 4).

Table 8
Numerical results for Example 4.6 on Mesh 1.

Mesh level	1	2	3	4	5
E_u	1.55×10^{-3}	3.92×10^{-4}	9.57×10^{-5}	2.53×10^{-5}	6.22×10^{-6}
R_u		1.92	2.21	2.01	2.02
E_q	2.29×10^{-2}	1.07×10^{-2}	4.91×10^{-3}	2.48×10^{-3}	1.23×10^{-3}
R_q		1.07	1.22	1.03	1.01
nitn	4.01	4.01	4.02	4.02	4.02

We test this problem on all the six mesh types. Convergence results of ICD are graphically depicted in Fig. 11. It indicates that the errors in discrete L^2-norm (resp. H^1-norm) achieve approximately second order (resp. first order) in this strong anisotropic problem. The detailed numerical results on Mesh 1 are presented in Table 6, where we observe that the coercivity parameters *Coer* are positive while the values of ρ are negative. The results on Mesh 2 to Mesh 6 are similar and are omitted here.

4.5. Mesh locking

This test as a benchmark can be found in [24,32]. Consider the purely Dirichlet boundary problem on a unit square domain $\Omega = [0,1] \times [0,1]$ with the diffusion tensor

$$\Lambda = \begin{pmatrix} 1 & 0 \\ 0 & \delta \end{pmatrix}.$$

The exact solution is $u(x,y) = \sin(\pi x)\exp^{-2\pi y\sqrt{1/\delta}}$, where $\delta = 10^6$. We use Mesh 5 and the numerical results are presented in Table 7. One can see that the convergence rates for both schemes are optimal in this test. In addition, we can see that the accuracy of ICD is better than that of LPeLSW. The profiles of the numerical solutions for the ICD scheme on the third and fourth mesh levels are shown in Fig. 12, which shows that the solution is almost constant in the y direction.

4.6. Nonlinear parabolic problem with mixed boundary conditions

Consider the following nonlinear problem

$$\begin{cases} \dfrac{\partial u}{\partial t} - \operatorname{div}(u\nabla u) = Q(x,y,t), & (x,y,t) \in \Omega \times (0,T], \\ u(x,y,0) = \dfrac{1}{2}\exp(-(x^2+y^2)), & (x,y) \in \Omega, \\ u\dfrac{\partial u}{\partial \boldsymbol{n}} = 0, & y = 0, x \in [0,1], t \in (0,T], \\ u = \dfrac{\exp(t-(x^2+1))}{1+\exp(t)}, & y = 1, x \in [0,1], t \in (0,T], \\ u\dfrac{\partial u}{\partial \boldsymbol{n}} = 0, & x = 0, y \in [0,1], t \in (0,T], \\ u = \dfrac{\exp(t-(1+y^2))}{1+\exp(t)}, & x = 1, y \in [0,1], t \in (0,T], \end{cases}$$

where $\Omega = [0,1] \times [0,1]$ and the exact solution is

$$u = \frac{\exp(t-(x^2+y^2))}{1+\exp(t)}.$$

This problem can be found in [35]. The nonlinear iteration will stop if

$$\|\mathbf{U}^{(s+1)} - \mathbf{U}^{(s)}\|_2 / \|\mathbf{U}^{(s)}\|_2 < \epsilon_{non},$$

where $\mathbf{U}^{(s+1)}$ (resp. $\mathbf{U}^{(s)}$) denotes the $s+1$-th (resp. s-th) error vectors and $\epsilon_{non} = 10^{-10}$. We choose the time step $\tau = 10^{-3}$ and the computation stops at $T = 0.1$. The numerical results on Mesh 1 ($\alpha = 0.35$) are shown in Table 8. One can see that the L^2-error and H^1-error are approximately

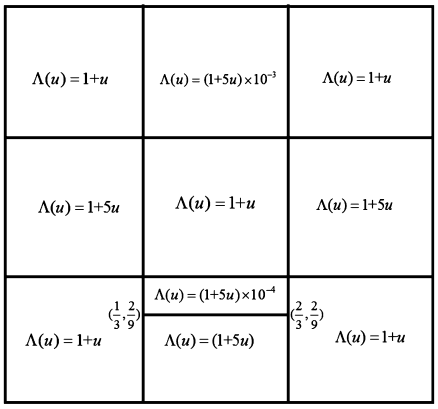

Fig. 14. Coefficients in the definition of diffusion tensor for Example 4.7.

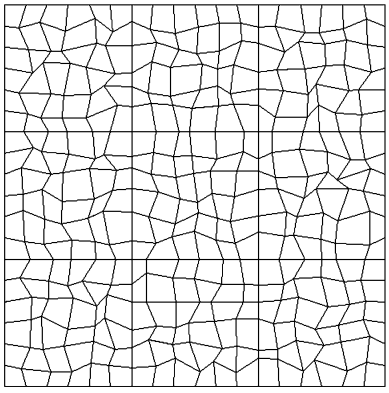

Fig. 15. The 18×18 random mesh with multiple discontinuities for Example 4.7.

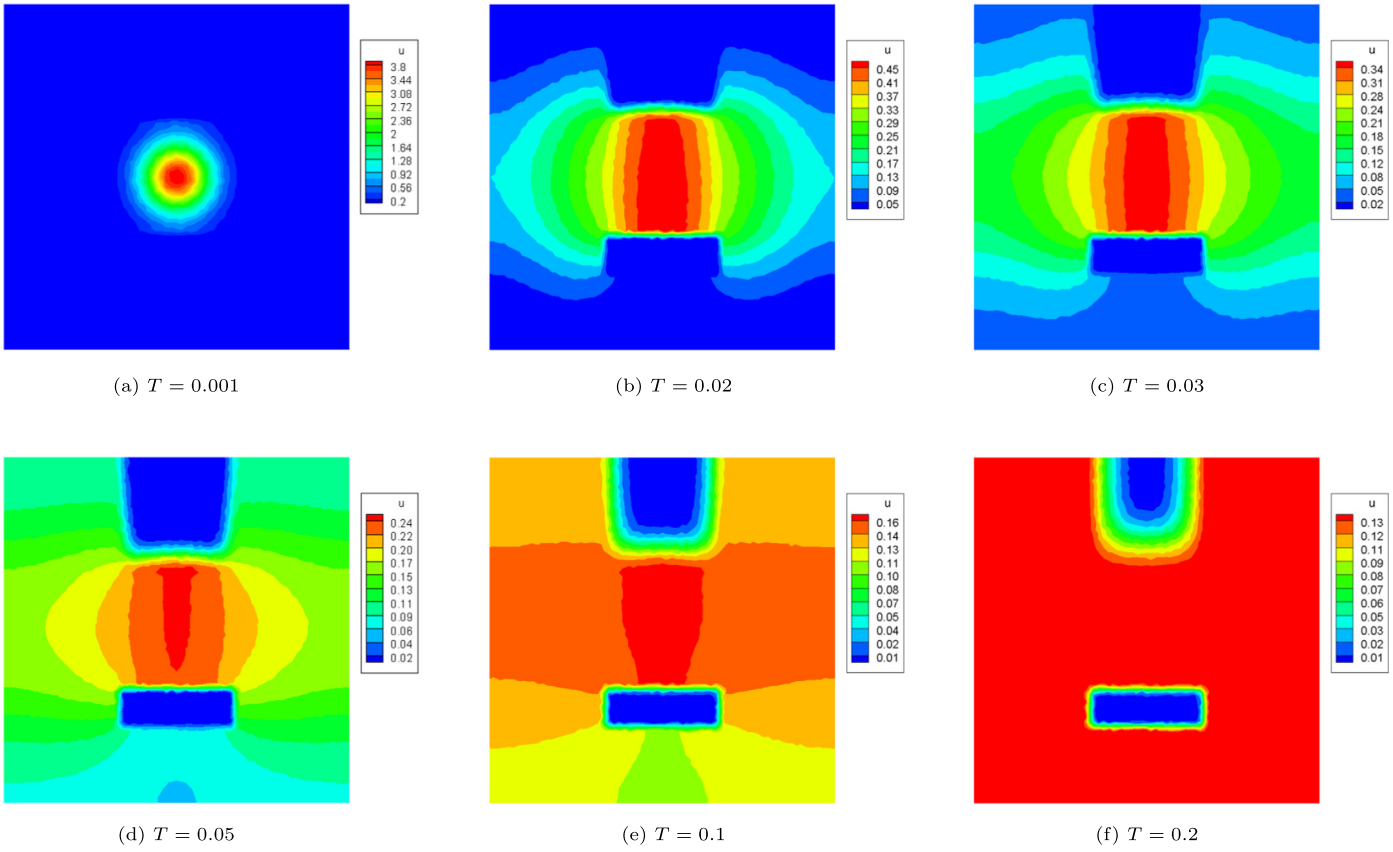

(a) $T = 0.001$ (b) $T = 0.02$ (c) $T = 0.03$

(d) $T = 0.05$ (e) $T = 0.1$ (f) $T = 0.2$

Fig. 16. Contours of the numerical solutions for Example 4.7 at different times.

second order and first order, respectively. In addition, the numbers of nonlinear iterations (`nitn`) are also given in Table 8. Solution contours on level 4 of Mesh 1 at time $T = 0.001$, $T = 0.01$, $T = 0.1$ are depicted in Fig. 13, respectively.

4.7. Nonlinear parabolic problem with pure Neumann boundary conditions

Finally, consider the following example

$$\begin{cases} \dfrac{\partial u}{\partial t} - \operatorname{div}(\Lambda(u)\nabla u) = 0, & (x,y,t) \in \Omega \times (0,T], \\ u(x,y,0) = 10\exp\left(\dfrac{a^2(x-c)^2+b^2(y-c)^2}{a^2(x-c)^2+b^2(y-c)^2-a^2b^2}\right), & a^2(x-c)^2 + b^2(y-c)^2 < a^2b^2, \\ u(x,y,0) = 0, & a^2(x-c)^2 + b^2(y-c)^2 \geq a^2b^2, \\ \Lambda(u)\dfrac{\partial u}{\partial \boldsymbol{n}} = 0, & (x,y) \in \partial\Omega, t \in (0,T], \end{cases}$$

where $a = b = 0.1$, $c = 0.5$. The computational domain $\Omega = [0,1] \times [0,1]$ is split into ten parts $\Omega = \bigcup_{i=1}^{10} \Omega_i$ with different diffusion coefficients, see Fig. 14. Assuming that domain Ω is adiabatic, we put a small hot disk in the middle and observe the effect of different diffusion coefficients on the temperature distribution in Ω. This example may also appear in some typical physical situations such as the incompressible flow in heterogeneous porous media [7].

The 72×72 random mesh (Mesh 1, $\alpha = 0.35$) shown in Fig. 15 is used. Here we require that the mesh lines should be aligned with the discontinuities. The time step is set to $\Delta t = 10^{-3}$ and the stopping tolerance of the nonlinear iteration is $\epsilon_{non} = 10^{-10}$. The numerical results at different times are shown in Fig. 16. The diffusion coefficients in regions $(\frac{1}{3}, \frac{2}{3}) \times (\frac{2}{9}, \frac{1}{3})$ and $(\frac{1}{3}, \frac{2}{3}) \times (\frac{2}{3}, 1)$ are small, which are equivalent to a heat transfer barrier, as can be obviously observed from Fig. 16. The number of nonlinear iterations starts with 15 steps and then 5 steps.

5. Conclusions

In this paper, we suggest a new method to construct the cell-centered finite volume discretization of the heterogeneous and anisotropic diffusion problems on polygonal meshes. Then, by this new method, we get a linear cell-centered scheme without auxiliary unknowns. Through a discrete functional approach, a sufficient condition is obtained to guarantee the coercivity of the new scheme theoretically. Numerical experiments show that the condition is effective in some cases, but fails in other cases, which indicates that this sufficient condition has great room for improvement. Based on the coercivity result and discrete Poincaré inequality, the stability of the new scheme can be proven. Numerical experiments show that the new linear cell-centered FV scheme maintains optimal convergence rate for the L^2-error and H^1-error on general polygonal meshes. We believe that the new interpolation-free cell-centered discretization method is a possible tool to construct nonlinear positive-preserving or extremum-preserving schemes on both 2D and 3D meshes, which constitutes the topic of our future study.

Data availability

Data will be made available on request.

Acknowledgements

The authors thank the anonymous reviewers for the carefully readings and valuable suggestions. This work was partially supported by the National Natural Science Foundation of China (Nos. 11871009, 12171048, 12271055), the foundation of CAEP (CX20210044) and the Foundation of LCP.

References

[1] I. Aavatsmark, An introduction to multipoint flux approximations for quadrilateral grids, Comput. Geosci. 6 (2002) 405–432.
[2] I. Aavatsmark, T. Barkve, O. Bøe, T. Mannseth, Discretization on unstructured grids for inhomogeneous, anisotropic media. I. Derivation of the methods, SIAM J. Sci. Comput. 19 (1998) 1700–1716.
[3] I. Aavatsmark, G.T. Eigestad, B.T. Mallison, J.M. Nordbotten, A compact multipoint flux approximation method with improved robustness, Numer. Methods Partial Differ. Equ. 24 (2008) 1329–1360.
[4] L. Agelas, D.A. Di Pietro, J. Droniou, The G method for heterogeneous anisotropic diffusion on general meshes, ESAIM: Math. Model. Numer. Anal. 44 (2010) 597–625.
[5] L. Agelas, R. Eymard, R. Herbin, A nine-point finite volume scheme for the simulation of diffusion in heterogeneous media, C.R. Acad. Sci. Paris, Ser. I 347 (2009) 673–676.
[6] B. Andreianov, F. Boyer, F. Hubert, Discrete duality finite volume schemes for Leray-Lions-type elliptic problems on general 2D meshes, Numer. Methods Partial Differ. Equ. 23 (2007) 145–195.
[7] F. Boyer, F. Hubert, Finite volume method for 2D linear and nonlinear elliptic problems with discontinuities, SIAM J. Numer. Anal. 46 (2008) 3032–3070.
[8] F. Brezzi, K. Lipnikov, M. Shashkov, Convergence of the mimetic finite difference method for diffusion problems on polyhedral meshes, SIAM J. Numer. Anal. 43 (2005) 1872–1896.
[9] F. Brezzi, K. Lipnikov, V. Simoncini, A family of mimetic finite difference methods on polygonal and polyhedral meshes, Math. Models Methods Appl. Sci. 15 (2005) 1533–1551.
[10] T. de M. Cavalcante, F.R.L. Contreras, P.R.M. Lyra, D.K.E. de Carvalho, A multipoint flux approximation with diamond stencil finite volume scheme for the two-dimensional simulation of fluid flows in naturally fractured reservoirs using a hybrid-grid method, Int. J. Numer. Methods Fluids 92 (2020) 1322–1351.
[11] A. Chernyshenko, Y. Vassilevski, A finite volume scheme with the discrete maximum principle for diffusion equations on polyhedral meshes, in: Finite Volumes for Complex Applications VII - Methods and Theoretical Aspects, Springer, 2014, pp. 197–205.
[12] F.R.L. Contreras, P.R.M. Lyra, M.R.A. Souza, D.K.E. de Carvalho, A cell-centered multipoint flux approximation method with a diamond stencil coupled with a higher order finite volume method for the simulation of oil-water displacements in heterogeneous and anisotropic petroleum reservoirs, Comput. Fluids 127 (2016) 1–16.
[13] Y. Coudière, J.-P. Vila, P. Villedieu, Convergence rate of a finite volume scheme for a two dimensional convection-diffusion problem, ESAIM: Math. Model. Numer. Anal. 33 (1999) 493–516.
[14] A. Danilov, Y. Vassilevski, A monotone nonlinear finite volume method for diffusion equations on conformal polyhedral meshes, Russ. J. Numer. Anal. Math. Model. 24 (2009) 207–227.
[15] N. Ding, Y. Zhang, D. Xiao, J. Wu, Z. Dai, L. Yin, Z. Gao, S. Sun, C. Xue, C. Ning, X. Shu, J. Wang, Theoretical and numerical research of wire array Z-pinch and dynamic hohlraum at IAPCM, Matter Radiat. Extrem. 1 (2016) 135–152.
[16] J. Droniou, Finite volume schemes for diffusion equations: introduction to and review of modern methods, Math. Models Methods Appl. Sci. 24 (2014) 1575–1619.
[17] J. Droniou, R. Eymard, A mixed finite volume scheme for anisotropic diffusion problems on any grid, Numer. Math. 105 (2006) 35–71.
[18] M.G. Edwards, Unstructured, control-volume distributed, full-tensor finite-volume schemes with flow-based grids, Comput. Geosci. 6 (2002) 433–452.
[19] R. Eymard, T. Gallouet, R. Herbin, Discretization of heterogeneous and anisotropic diffusion problems on general nonconforming meshes SUSHI: a scheme using stabilization and hybrid interfaces, IMA J. Numer. Anal. 30 (2010) 1009–1043.
[20] R. Eymard, R. Herbin, C. Guichard, Small-stencil 3D schemes for diffusive flows in porous media, Math. Model. Numer. Anal. 46 (2012) 265–290.
[21] Z. Gao, J. Wu, A second-order positivity-preserving finite volume scheme for diffusion equations on general meshes, SIAM J. Sci. Comput. 37 (2015) A420–A438.
[22] Z. Gao, J. Wu, A linearity-preserving cell-centered scheme for the heterogeneous and anisotropic diffusion equations on general meshes, Int. J. Numer. Methods Fluids 67 (2011) 2157–2183.
[23] Z. Gao, J. Wu, A small stencil and extremum-preserving scheme for anisotropic diffusion problems on arbitrary 2D and 3D meshes, J. Comput. Phys. 250 (2013) 308–331.
[24] R. Herbin, F. Hubert, Benchmark on discretization schemes for anisotropic diffusion problems on general grids, in: R. Eymard, J.-M. Hérard (Eds.), Finite Volumes for Complex Applications V, Wiley, 2008, pp. 659–692.
[25] F. Hermeline, A finite volume method for the approximation of diffusion operators on distorted meshes, J. Comput. Phys. 160 (2000) 481–499.
[26] D. Li, H. Shui, M. Tang, On the finite difference scheme of two-dimensional parabolic equation in a non-rectangular mesh, J. Numer. Methods Comput. Appl. 1 (1980) 217–224 (in Chinese).
[27] K. Lipnikov, M. Shashkov, D. Svyatskiy, Y. Vassilevski, Monotone finite volume schemes for diffusion equations on unstructured triangular and shape regular polygonal meshes, J. Comput. Phys. 227 (2007) 492–512.
[28] K. Lipnikov, D. Svyatskiy, Y. Vassilevski, Interpolation-free monotone finite volume method for diffusion equations on polygonal meshes, J. Comput. Phys. 228 (2009) 703–716.
[29] K. Lipnikov, D. Svyatskiy, Y. Vassilevski, A monotone finite volume method for advection-diffusion equations on unstructured polygonal meshes, J. Comput. Phys. 229 (2010) 4017–4032.
[30] K. Lipnikov, D. Svyatskiy, Yu. Vassilevski, Minimal stencil finite volume scheme with the discrete maximum principle, Russ. J. Numer. Anal. Math. Model. 27 (4) (2012) 369–386.
[31] K. Lipnikov, D. Svyatskiy, Y. Vassilevski, Anderson acceleration for nonlinear finite volume scheme for advection-diffusion problems, SIAM J. Sci. Comput. 35 (2013) A1120–A1136.
[32] G. Manzini, M. Putti, Mesh locking effects in the finite volume solution of 2-D anisotropic diffusion equations, J. Comput. Phys. 220 (2007) 751–771.
[33] W. Mao, Y. Zhu, M. Ye, X. Zhang, J. Wu, J. Yang, A new quasi-3-D model with a dual iterative coupling scheme for simulating unsaturated-saturated water flow and solute transport at a regional scale, J. Hydrol. 602 (2021) 126780.
[34] S. Miao, J. Wu, A nonlinear correction scheme for the heterogeneous and anisotropic diffusion problems on polygonal meshes, J. Comput. Phys. 448 (2022) 110729.
[35] S. Miao, Y. Yao, G. Lv, An efficient parallel iteration algorithm for nonlinear diffusion equations with time extrapolation techniques and the Jacobi explicit scheme, J. Comput. Phys. 441 (2021) 110435.
[36] J. Morel, R. Roberts, M. Shashkov, A local support-operators diffusion discretization scheme for quadrilateral r-z meshes, J. Comput. Phys. 144 (1998) 17–51.
[37] V. Mousseau, D. Knoll, New physics-based preconditioning of implicit methods for non-equilibrium radiation diffusion, J. Comput. Phys. 190 (2003) 42–51.
[38] K. Nikitin, Y. Vassilevski, A monotone nonlinear finite volume method for advection-diffusion equations on unstructured polyhedral meshes in 3D, Russ. J. Numer. Anal. Math. Model. 25 (2010) 335–358.
[39] C. Le Potier, A second order in space combination of methods verifying a maximum principle for the discretization of diffusion operators, C. R. Math. Acad. Sci. Paris 358 (2020) 89–95.
[40] C. Le Potier, Schéma volumes finis monotone pour des opérateurs de diffusion fortement anisotropes sur des maillages de triangles non structurés, C. R. Acad. Sci. Paris, Ser. I 341 (2005) 787–792.
[41] M. Schneider, L. Agélas, G. Enchéry, B. Flemisch, Convergence of nonlinear finite volume schemes for heterogeneous anisotropic diffusion on general meshes, J. Comput. Phys. 351 (2017) 80–107.
[42] M. Schneider, D. Gläser, B. Flemisch, R. Helmig, Comparison of finite-volume schemes for diffusion problems, Oil Gas Sci. Technol. - Rev. IFP Energ. Nouv. 73 (2018) 82.
[43] M. Shashkov, S. Steinberg, Support-operator finite-difference algorithms for general elliptic problems, J. Comput. Phys. 118 (1995) 131–151.

[44] S. Su, Q. Dong, J. Wu, A decoupled and positivity-preserving discrete duality finite volume scheme for anisotropic diffusion problems on general polygonal meshes, J. Comput. Phys. 372 (2018) 773–798.
[45] W. Sun, J. Wu, X. Zhang, A family of linearity-preserving schemes for anisotropic diffusion problems on arbitrary polyhedral grids, Comput. Methods Appl. Mech. Eng. 267 (2013) 418–433.
[46] K.M. Terekhov, B.T. Mallison, H.A. Tchelepi, Cell-centered nonlinear finite-volume methods for the heterogeneous anisotropic diffusion problem, J. Comput. Phys. 330 (2017) 245–267.
[47] Y. Vassilevski, K. Terekhov, K. Nikitin, I. Kapyrin, Parallel Finite Volume Computation on General Meshes, Springer, Switzerland, 2020.
[48] D. Vidović, M. Dotlić, M. Dimkić, M. Pušić, B. Pokorni, Convex combinations for diffusion schemes, J. Comput. Phys. 246 (2013) 11–27.
[49] D. Vidović, M. Dotlić, M. Pušić, Accelerated non-linear finite volume method for diffusion, J. Comput. Phys. 230 (2011) 2722–2735.
[50] J. Wu, Z. Dai, Z. Gao, G. Yuan, Linearity preserving nine-point schemes for diffusion equation on distorted quadrilateral meshes, J. Comput. Phys. 229 (2010) 3382–3401.
[51] J. Wu, Z. Gao, Interpolation-based second-order monotone finite volume schemes for anisotropic diffusion equations on general grids, J. Comput. Phys. 275 (2014) 569–588.
[52] J. Wu, Z. Gao, Z. Dai, A stabilized linearity-preserving scheme for the heterogeneous and anisotropic diffusion problems on polygonal meshes, J. Comput. Phys. 231 (2012) 7152–7169.
[53] J. Wu, Z. Gao, Z. Dai, A vertex-centered linearity-preserving discretization of diffusion problems on polygonal meshes, Int. J. Numer. Methods Fluids 81 (2016) 131–150.
[54] H. Xie, X. Xu, C. Zhai, H. Yong, A positivity-preserving finite volume scheme with least square interpolation for 3D anisotropic diffusion equation, J. Sci. Comput. 89 (2021) 53.
[55] G. Yuan, Z. Sheng, Monotone finite volume schemes for diffusion equations on polygonal meshes, J. Comput. Phys. 227 (2008) 6288–6312.
[56] W. Zhang, M. Kobaisi, Cell-centered nonlinear finite-volume methods with improved robustness, SPE J. 25 (2020) 288–309.